

See discussions, stats, and author profiles for this publication at: <https://www.researchgate.net/publication/350482413>

# Spatial Aliasing and Three-Component Seismic Sensors

Article in *Geophysics* · March 2021

DOI: 10.1190/geo2020-0172.1

---

CITATIONS

5

READS

108

1 author:



Jakob Haldorsen

MagiQ Technologies

96 PUBLICATIONS 643 CITATIONS

SEE PROFILE

# Spatial Aliasing and Three-Component Seismic Sensors

Geophysics, 86, No. 4, pp. V255-V267, <https://library.seg.org/doi/10.1190/geo2020-0172.1>

This copy was produced December 28, 2021

Jakob B.U. Haldorsen\*

## ABSTRACT

Temporal aliasing occurs when a waveform is sampled with less than two points per time period for a signal at a given frequency. This insufficiently sampled frequency will incorrectly be mapped into a lower (aliased) frequency. Analogous to this, spatial aliasing is said to occur when a propagating waveform is measured at spatial intervals larger than half the wavelength of any given signal in that waveform. Temporally aliased frequencies cannot be recovered with standard methods. On the other hand, we argue that "spatial aliasing" can be viewed as an expression of a non-uniqueness for estimating the direction of the propagation for signal at a given frequency, and that spatial aliasing may be overcome when three-component seismic sensors are used. Realizing this allows for using higher frequencies, and therefore enables the generation of higher resolution images from the data. This is particularly useful for borehole-seismic data which tend to contain higher frequencies than surface-seismic data, but does require that an array of three-component sensors is used, or that an array of less expensive single-component sensors is supplement by three-component sensors.

## INTRODUCTION

Aliasing is a well-known problem in signal rendering, and relates to frequency ambiguity. Frequency ambiguity can occur when discrete elements have been used to capture a continuous signal. Spatial aliasing of an angular frequency can occur when a discrete array of sensors is used to measure a propagating wavefield. To avoid temporal aliasing, the signal must be sampled at at-least twice the highest frequency in the continuous signal. To avoid spatial aliasing, the distance between adjacent sensors in the measuring array must be smaller than half the spatial wavelength of a propagating wavefield. Conversely, for

a fixed sampling rate, the highest frequency, temporal or spatial, in the analog signal can be no higher than a half of the sampling rate. Signal at a frequency that is insufficiently sampled will incorrectly be mapped into a lower (aliased) frequency.

We will review the Fourier transforms, in one to four dimensions, pointing to that these transforms essentially project an observed function or wavefields onto harmonic functions, the eigenfunctions for harmonic oscillators. In the 1D case, with a single simple harmonic oscillator in the system to which we apply our discrete measurements, we may or may not be able to measure the true frequency for the oscillator, depending on the sampling of the motion of the oscillator. This stems from the fundamental ambiguity in the frequency reproducing a given discretized function. This ambiguity gives temporal aliasing: instead of a definite frequency, we get a choice of frequencies. From this choice, we normally choose the frequency with the smallest value which may or may not be the correct value.

For higher-dimensional measurements, the traditional process is to regard the wavefield decomposition performed by the Fourier transform as three or four orthogonal 1D transforms, essentially not taking the physics of propagating P- or S-waves into consideration. We argue that the inherent ambiguities in the 1D Fourier transforms gives rise to spatial aliasing, and that spatial aliasing can be viewed as an expression of a non-uniqueness for estimating the direction of propagation for signal at a given frequency. This ambiguity may be overcome when three-component (3C) seismic sensors are used. Realizing this will allow for using higher frequencies, and therefore enable generation of higher resolution images from the data. This is particularly useful for borehole-seismic data which tend to contain higher frequencies than surface-seismic data. With the new DAS technology (e.g., Farhadroushan et al., 2009), one can relatively inexpensively build large arrays of single-component sensors; however spatial aliasing will be a problem if only one single component is measured at each sensor. Complementing a DAS array with sparsely distributed 3C sensors would resolve the directional ambiguities of DAS data.

The objective of this study is to support work already pub-

\*MagiQ Technologies, Somerville, MA, USA

lished (e.g., Leaney and Esmersoy (1989) on plane-wave decomposition of borehole-seismic data, Haldorsen (2002) and Haldorsen and Jahren (2020) on elastic migration of borehole-seismic data, and Artman et al. (2010) and Haldorsen et al. (2013a) on migration approaches to locating the hypocenter of a microseismic event), essentially having demonstrated that the components of a complicated wavefield can be separated and estimated despite being spatially aliased, provided that the polarization of the wavefield components are used.

## THE FOURIER TRANSFORM

The Fourier transform of a function  $a(t)$  is defined by (e.g., Bracewell, 1978)

$$A(\omega) = \int dt e^{-i\omega t} a(t), \quad (1)$$

Assuming that a given waveform is composed of a sum of monochromatic wavefields, the Fourier transform projects the time series onto an orthonormal set of basis functions  $e^{-i\omega t}$ . In applications to propagating wavefields, the variable  $t$  is time measured in seconds, and  $\omega$  is angular frequency measured in radians per second. Instead of angular frequency  $\omega$ , it is common to use the related quantity frequency  $f = \frac{\omega}{2\pi}$ , measured in cycles per second.

For a time series of finite length  $T = N\Delta t$ , sampled at discrete times at a fixed interval of  $\Delta t$ , equation 1 takes the form:

$$\begin{aligned} A(\omega) &= \int dt e^{-i\omega t} a(t) \delta(t - t_n), \\ &= \sum_{n=0}^{N-1} e^{-i\omega n\Delta t} a(n\Delta t), \end{aligned} \quad (2)$$

where  $\delta$  is the Dirac delta function. The algorithm normally used to calculate this Fourier transform assumes that the series is infinitely periodic at a period  $T$ , giving a set of discrete angular frequencies  $\omega_n$  at which the function  $A(\omega) \in \{A(n\Delta\omega)\}$  is sampled. These angular frequencies  $\omega_n$  (with  $-\omega_{Nq} \leq \omega_n < \omega_n$ ) are separated by  $\Delta\omega = \frac{2\pi}{T}$ .  $\omega_{Nq} = \frac{\pi}{\Delta t}$  is the angular "Nyquist frequency". From the discrete sampling in the time domain, it follows that the transformed function is also periodic in the  $\omega$  domain. The transformed function  $A(\omega)$  is normally truncated at the "Nyquist frequency".

With the elements  $a(t_n)$  being real-valued, it follows straightforwardly from equation 2 that  $A(-\omega) = A^*(\omega)$  (with  $A^*$  meaning the "complex conjugate" of  $A$ ), and  $A(\omega_{Nq}) = A(\omega = 0)$ , assuring that the real-valued time-domain series and the complex-valued frequency-domain series contain the same number of independent variables.

Inversely, from a  $\omega$ -domain signal  $A(\omega)$ , we get the time-domain series from

$$a(t) = \frac{1}{N} \sum_{n=0}^{N-1} e^{itn\Delta\omega} A(n\Delta\omega). \quad (3)$$

The normalization factor  $\frac{1}{N} = \frac{\Delta t}{T} = \frac{\Delta\omega}{\Omega}$  in equation 3 assures the preservation of amplitudes in a forward, followed by an inverse transform. I use the symbol  $\Omega (= N\Delta\omega = 2\omega_{Nq})$  for the full range of angular frequencies.

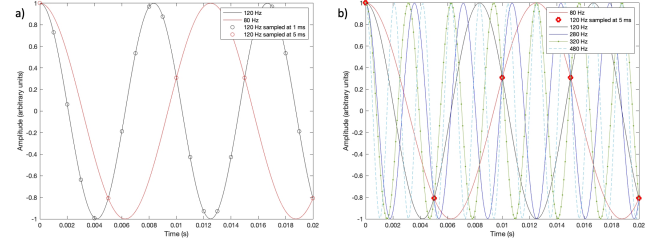


Figure 1: A time series consisting of a monochromatic signal at 120 Hz. In a), the black circles indicate time along the curve at 0.001 s interval, and the red circles indicate time for every 0.005 s. The red curve shows a time series that is consistent with the red circles within the frequency band from zero frequency to the maximum unique temporal frequency,  $f_{Nq} = \frac{1}{2\Delta t}$ , the "Nyquist" frequency. For  $\Delta t = 0.005$  s,  $f_{Nq}$  is 100 Hz, and the "aliased", apparent frequency is  $f_{alias} = 2f_{Nq} - f = 80$  Hz. In b), I have plotted as well the waveforms for frequencies of 80, 120, 280, 320, and 480 Hz. These all go through the red circles, and therefore are all consistent with the measurements.

## TEMPORAL ALIASING

A monochromatic waveform at temporal frequency  $\omega_0$ , can be described by

$$A(\omega) = g(\omega_0), \quad (4)$$

which can be inserted into equation 3 to give

$$a(t) = \frac{1}{N} g(\omega_0) e^{i\omega_0 t}. \quad (5)$$

Figure 1 shows a monochromatic waveform at a frequency  $f = 120$  Hz, with  $f = \frac{\omega}{2\pi}$ . For simplicity of arguments, I have left out the normalization factor  $\frac{1}{N}$  in the plots and in the following discussion. This waveform may be sampled sufficiently or insufficiently densely. Whereas the black circles indicate time along the curve at 0.001 s interval, the red circles indicate time for every 0.005 s. The red curve shows a time series that is consistent with the red circles within the frequency band from zero frequency to the maximum unique temporal frequency for sampling at  $\Delta t = 0.005$  s. The maximum unique frequency  $f_{Nq} = \frac{1}{2\Delta t}$ . For  $\Delta t = 0.005$  s,  $f_{Nq}$  is 100 Hz, and the "aliased", apparent frequency is  $f_{alias} = 2f_{Nq} - f = 80$  Hz.

In Figure 1, I have as well plotted the waveforms for frequencies of 80, 120, 280, 320, and 480 Hz. These all go through the red circles, and therefore are all consistent with the measurements. It is clear that temporal aliasing is fatal: Once aliased, the frequency at which the waveform actually vibrated cannot be recovered.

## SPATIAL ALIASING

Spatial aliasing relates to measuring a propagating wave at distinct locations in space. However, the manifestation of spatial aliasing is different from that of temporal aliasing, as we shall see in what follows. We will first consider the 2D Fourier transform, introducing the concept of spatial aliasing - before we turn to the more general 4D transform (4D for one temporal

and three spatial dimensions), possibly offering a resolution to the problem of spatial aliasing.

## 2D Fourier Transform

The commonly used 2D Fourier transform decomposes a wavefield recorded by a linear array of receivers (most often regular) into waves propagating in a 1D linear space. These 1D waves are thought of as substitutes for plane waves. The 2D Fourier transform can be implemented as two subsequent 1D Fourier transforms: first a frequency decomposition for single traces recorded by each receiver, then a transform for constant frequencies from a set of 1D spatial coordinates to a set of 1D wavenumbers. For a continuous linear waveform  $a(t, x)$  measured by a continuous linear array along  $x$ , we can write the 2D Fourier transform as follows:

$$\begin{aligned} A(\omega, k) &= \int dx dt e^{i(kx - \omega t)} a(t, x), \\ &= \int dx e^{ikx} \int dt e^{-i\omega t} a(t, x), \\ &= \int dx e^{i\omega sx} \int dt e^{-i\omega t} a(t, x), \end{aligned} \quad (6)$$

where  $\omega = 2\pi f$  again denotes the angular frequency, and  $k = \omega s$  is the angular wavenumber, with  $s$  being the slowness (the inverse of velocity) for the propagating wavefield. The angular wavenumber is the Fourier-domain dual to space. Instead of an angular wavenumber  $k$  and an angular frequency  $\omega$ , which are measured in radians per unit distance or time, it is not uncommon to instead use the wavenumber  $\eta = \frac{k}{2\pi}$ , and frequency  $f = \frac{\omega}{2\pi}$ , measured in cycles per unit distance or time.

When the wavefield is sampled at regular, discrete times  $t_n = n\Delta t$ , and at regular, discrete points in space  $x_m = m\Delta x$  along a linear array of sensors, we have

$$A(\omega, k) = \sum_{m=0}^{M-1} e^{i\omega sm\Delta x} \sum_{n=0}^{N-1} e^{-i\omega n\Delta t} a(n\Delta t, m\Delta x). \quad (7)$$

Assuming that the wavefield is periodic both in space and time,  $\omega$  will be sampled at discrete frequencies  $\Delta\omega = \frac{2\pi}{T}$ , up to a maximum of  $\pm\frac{\pi}{\Delta t}$ , where  $T = N\Delta t$ , the temporal period, and the angular wavenumber  $k$  will be sampled at  $\Delta k = \frac{2\pi}{X}$ , up to a maximum wavenumber of  $\pm\frac{\pi}{\Delta x}$ , where  $X = M\Delta x$  is the total length of the linear array. In the context of wavefields propagating in a 3D space, and measured by a linear array of sensors, equation 6 should be seen as relating the measurements to projections of the 3D wavefield parameters - such as the wavefield slowness vector - onto the 1D sensor array.

Like in the previous section, the symmetry  $A(-\omega, x) = A^*(\omega, x)$  reduces the bandwidth for independent values of  $\omega$  to the semi-closed interval from 0 to  $\omega_{NQ}$ , with  $\omega_{NQ} = \frac{\pi}{\Delta t}$ . As  $A(\omega, x)$  is complex-valued, there is no corresponding reduction in bandwidth for  $k$ .

If the wavefield is a superposition of  $J$  elemental plane waves with amplitudes  $g_j(\omega)$  and propagating at slownesses  $s_j$ :

$$a(t, x) = \frac{1}{N} \sum_{j,\omega} g_j(\omega) e^{-i\omega(s_j x - t)}. \quad (8)$$

The discretized function  $a(n\Delta t, m\Delta x)$  is obtained by introducing discrete sampling points  $t_n = n\Delta t$  and  $x_m = m\Delta x$  into equation 8. Limiting the discretized function to a single, monochromatic wavefield at angular frequency  $\omega_0$ , propagating at slowness  $s_0$ , and substituting this into equation 7, we have:

$$\begin{aligned} A(\omega, k(s)) &= \sum_{m=0}^{M-1} e^{i\omega sm\Delta x} \frac{1}{N} \sum_{n=0}^{N-1} e^{-i\omega n\Delta t} g(\omega_0) e^{-i\omega(s_0 m\Delta x - n\Delta t)}, \\ &= g(\omega_0) \sum_{m=0}^{M-1} e^{i\omega sm\Delta x} e^{-i\omega s_0 m\Delta x} \frac{1}{N} \sum_{n=0}^{N-1} e^{-i\omega n\Delta t} e^{i\omega n\Delta t}, \\ &= g(\omega_0) \sum_{m=0}^{M-1} e^{i\omega(s - s_0)m\Delta x}. \end{aligned} \quad (9)$$

Assuming that the propagators for the plane-wave components are approximately orthogonal, in the sense that  $\sum_{m=0}^{M-1} e^{i\omega(s - s_0)m\Delta x} \approx M$  for  $s = s_0$  and  $\sum_{m=0}^{M-1} e^{i\omega(s - s_0)m\Delta x} \approx 0$  for  $s \neq s_0$ , we find that the wavefield component  $g(\omega_0)$  can be estimated from the Fourier-domain amplitude at angular wavenumber  $k_0 = k(s_0)$ , divided by the number of element in the spatial sensor array, as follows:

$$g(\omega_0) = \frac{1}{M} A(\omega, k_0). \quad (10)$$

If  $k_0$  is larger than the largest value that can be recorded by the 2D Fourier transform ( $\pm\frac{\pi}{\Delta x}$ ), the estimate of the wavenumber will be aliased.

Figure 2 shows a 120 Hz monochromatic waveform sampled by 11 receivers in a linear receiver array with the receivers 15 m apart. The receivers are single component (e.g., pressure) sensors. The wavefield is propagating down along the array, at a velocity of 5000 m/s. As customary, the 2D Fourier analysis of these data has been done in terms of frequency  $f$  and wavenumber  $\eta$ , with  $\eta = \frac{k}{2\pi} = \frac{\omega s}{2\pi} = fs$ . With a spatial sampling interval of 15 m, the maximum (Nyquist) wavenumber is  $\eta_{NQ} = \pm\frac{1}{2\Delta x} = \pm\frac{1}{30} \text{ m}^{-1}$ . It is obvious that there are more than one solution to following a constant phase on the waveforms recorded by the different sensors. The 2D Fourier analysis shows one single point of high amplitude at  $f = 120 \text{ Hz}$ , and  $\eta \approx 0.025 \text{ m}^{-1}$ . This value is approximately correct, corresponding to a velocity  $v = \frac{1}{s} = \frac{f}{\eta} \approx \frac{-120 \text{ Hz}}{0.025 \text{ m}^{-1}} \approx 4800 \text{ m/s}$  down (the +z axis is pointing down). It just so happens that this correct value is inside the interval of unique wavenumbers  $\eta \in [-\frac{1}{30}, \frac{1}{30}] \text{ m}^{-1}$ .

If we increase the slowness (slower velocity), the picture changes. Figure 3 shows the 120 Hz monochromatic waveform sampled by the same linear receiver array, but propagating at 2750 m/s down along the array. The 2D Fourier analysis shows one single point of high amplitude at  $f = 120 \text{ Hz}$ , and  $\eta \approx -0.027 \text{ m}^{-1}$ , corresponding to a velocity  $v = \frac{1}{s} = \frac{\omega}{k} = \frac{f}{\eta} \approx \frac{120 \text{ Hz}}{-0.027 \text{ m}^{-1}} \approx -4400 \text{ m/s}$ , up along the array, instead of the correct value for  $\eta \approx 0.045 \text{ m}^{-1}$ , which is higher than the maximum unique value for  $\eta$  of  $0.033 \text{ m}^{-1}$ .

Again, the time-domain display in Figure 3 clearly shows the ambiguity of picking traveltimes: instead of choosing the higher value for  $\eta$  (slower propagation velocity) in the correct direction, the assumptions inherent in the Fourier transform

## Aliasing 3C Data

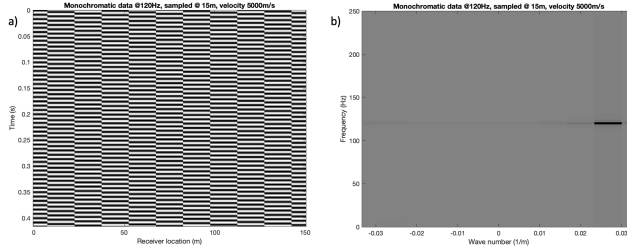


Figure 2: a) a monochromatic wavefield at a frequency of  $120\text{ Hz}$ , sampled by a vertical linear array of 11 single-component receivers at  $15\text{ m}$  interval. The display shows data recorded by the single-component receivers, with the shallowest receiver on the left. The wavefield is propagating down along the array at a velocity of  $5000\text{ m/s}$ . b) a 2D Fourier transform of these waveforms, showing a single component at frequency  $f = 120\text{ Hz}$  and moving down along the array at the wavenumber  $\eta \approx 0.025\text{ m}^{-1}$ .

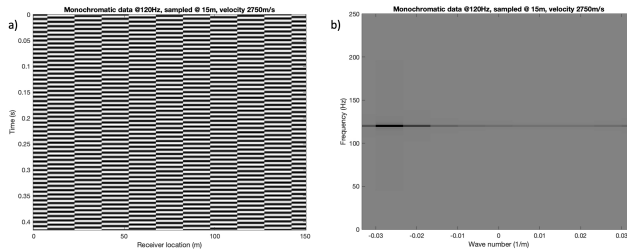


Figure 3: a) a monochromatic wavefield at a frequency of  $120\text{ Hz}$ , sampled by a vertical linear array of 11 single-component receivers spaced  $15\text{ m}$  apart. The shallowest receiver is on the left. The wavefield is propagating down along the array at a velocity of  $2750\text{ m/s}$ . b) a 2D Fourier analysis of these waveforms, showing a single component at frequency  $f = 120\text{ Hz}$  and appearing to be moving up along the array at the wavenumber  $\eta \approx -0.027\text{ m}^{-1}$ .

forces the choice of the lower value for  $\eta$  (faster propagation velocity) in the wrong direction. However, as we will see in the next section, this problem can be overcome by explicitly using the polarization direction measured by a 3C geophone or accelerometer.

## Multi-Component Measurement of Particle Motion

The 4D (time and space) Fourier transform decomposes the recorded wavefield into plane waves propagating in a 3D space. Similar to the previous section, we have

$$A(\omega, \mathbf{x}) = \int d^3\mathbf{x} dt e^{i(\mathbf{k}\cdot\mathbf{x}-\omega t)} a(t, \mathbf{x}), \quad (11)$$

where  $\omega = 2\pi f$  again denotes the angular frequency, and the angular wavenumber vector is  $\mathbf{k} = \omega\mathbf{s}$ , with  $\mathbf{s}$  being the slowness vector for the propagating wavefield.

When the wavefield is sampled at discrete times  $t_n = n\Delta t$ ,

and at discrete points  $\mathbf{x}$ , we have:

$$\begin{aligned} A(\omega, \mathbf{k}) &= \int d^3\mathbf{x} e^{i\mathbf{k}\cdot\mathbf{x}} \sum_{n=0}^{N-1} e^{-i\omega n\Delta t} a(n\Delta t, \mathbf{x}), \\ &= \sum_m e^{i\mathbf{k}\cdot\mathbf{x}_m} A'(\omega, \mathbf{x}_m). \end{aligned} \quad (12)$$

Although equation 12 is expressed in terms of three-component vectors  $\mathbf{x}_m$  and  $\mathbf{k}$ , the product  $\mathbf{k} \cdot \mathbf{x}_m$  projects  $\mathbf{k}$  onto the linear array at  $\mathbf{x}_m = (m-1)\Delta\mathbf{x}$ , and the result is rotationally symmetric around the straight line  $\{\mathbf{x}_m\}$ . However, with 3C measurements of the particle motion induced by a passing wave, one can apply a much tighter constraint to the data than what is provided by the projections in equations 11 and 12. For compressional waves, the polarization is aligned with the direction of propagation. For shear waves, the polarization and direction of propagation are mutually perpendicular. Assuming that we are dealing with compressional waves, the data vector  $\mathbf{a}(t, \mathbf{x})$  - measuring the particle motion at discrete points  $\mathbf{x}$  - should be aligned at each instance of time with the unit vector  $\mathbf{e}_k = \frac{\mathbf{k}}{|\mathbf{k}|}$ , pointing along  $\mathbf{k}$  in the direction of wavefield propagation:

$$\mathbf{a}(t, \mathbf{x}) = a(t, \mathbf{x}) \mathbf{e}_k, \quad (13)$$

or, projected onto the unit vector  $\mathbf{e}_k$ :

$$a(t, \mathbf{x}) = \mathbf{e}_k \cdot \mathbf{a}(t, \mathbf{x}). \quad (14)$$

Using equation 14, we can rewrite equation 12 in terms of angular frequency  $\omega$  and the slowness vector  $\mathbf{s}$  - a function of velocity ( $v$ ), and the propagation direction polar and azimuth angles  $\theta$  and  $\phi$ :

$$A(\omega, \mathbf{s}(v, \theta, \phi)) = \sum_m e^{i\omega \mathbf{s} \cdot \mathbf{x}_m} \sum_n e^{i\omega t} \mathbf{e}_k \cdot \mathbf{a}(t_n, \mathbf{x}_m), \quad (15)$$

i.e., the energy  $|A(\omega, \mathbf{s}(v, \theta, \phi))|^2$  of a particular component of the wavefield can be estimated from the result of stacking the data recorded at the individual receivers (the  $\sum_m$  over  $M$  receivers) after first projecting them onto the slowness vector in the direction considered - then, secondly, performing a Fourier transform from time to frequency - and then, thirdly, applying a time shift (the operator  $e^{i\omega \mathbf{s} \cdot \mathbf{x}_m}$  applied to the frequency-domain data, shifts the time-domain data by the time  $\mathbf{s} \cdot \mathbf{x}_m$ ).

Significant plane-wave components in the data will give peaks in the distribution of  $|A(\omega, \mathbf{s}(v, \theta, \phi))|^2$  for the parameters describing these components. All times and coordinates are given relative to unknown references. However, as long as these unknown references in time and space are the same for all recorded traces, their actual values will not affect the amplitudes of the stacks.

If one measures only a single component of the wavefield (e.g., pressure), there is no meaningful way of making the analyses described by equation 15. With only one measured component, there are no constraints on the components of the wavenumber vector  $\mathbf{k}$  transverse to the direction of the linear array. With three-component sensors, we essentially measure the direction of the  $\mathbf{k}$  vector in 3D space. To demonstrate the power of making a directional measurement, I have added two more

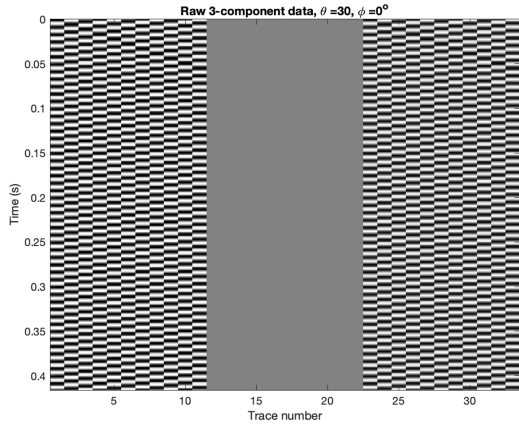


Figure 4: A monochromatic wavefield at a frequency of  $120\text{ Hz}$ , sampled by a vertical linear array of 11 three-component receivers spaced  $15\text{ m}$  apart. The display shows all horizontal (x) receivers, followed by all horizontal (y) receiver, and all vertical (z) receivers. The shallowest receiver is on the left. The wavefield is propagating down along receiver array at an apparent velocity of  $2750\text{ m/s}$ . The wavefield is propagating in the  $(x, z)$  plane (azimuth  $\phi = 0^\circ$ ), at a polar angle of  $\theta = 30^\circ$ .

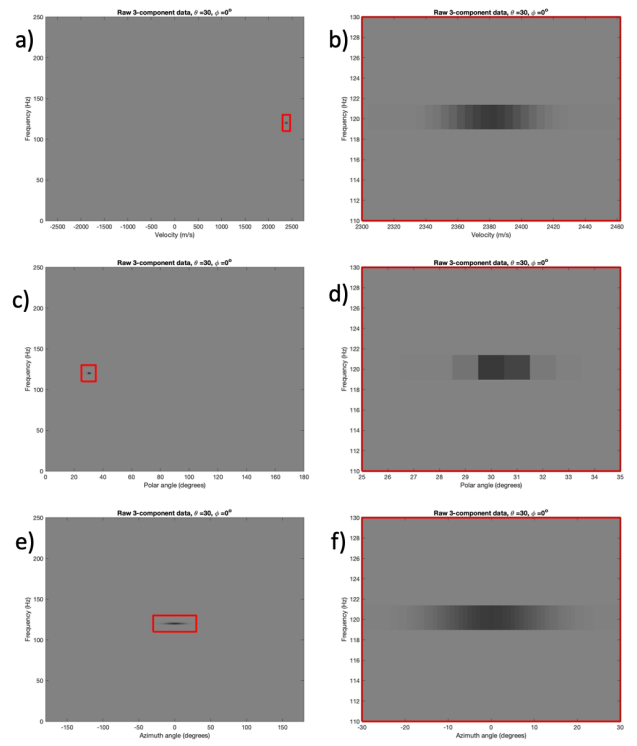


Figure 5: Orthogonal sections through the 4D hypercube  $A(f, \mathbf{s}(v, \theta, \phi))$  from equation 15. Along the right edge of the figure (subplots b, d, and f)) are shown zoomed-in images around the maximum in the larger plots on the left (subplots a, c, and e)). These sections indicate that the wavefield consists of one single component at frequency  $f = 120\text{ Hz}$ , propagating in the direction  $\theta = 30^\circ$  and  $\phi = 0^\circ$  at a speed of  $v = 2381\text{ m/s}$  (i.e., down at and angle of  $30^\circ$  with the vertical axis, at an apparent velocity of  $v = 2750\text{ m/s}$ ).

components to the  $120\text{ Hz}$  monochromatic, spatially aliased wavefield shown in Figure 3. The 3C data (in Figure 4) represent a compressional wavefield, propagating at a polar angle  $\theta = 30^\circ$  along the  $(xz)$  plane (azimuth  $\phi = 0^\circ$ ). The apparent velocity, measured from the time-lag from one 3C receiver to the next, is  $2750\text{ m/s}$  (the propagation velocity in 3D space is  $2750\text{ m/s} \cos 30^\circ = 2382\text{ m/s}$ ). Whereas the 2D Fourier analysis of the vertical components only, gives the flawed  $fk$  spectra shown in Figure 3, with three components we can perform the plane-wave analysis of equation 15. Figure 5 shows mutually perpendicular sections through the 4D hypercube of the Fourier-domain amplitudes  $A(f, \mathbf{s}(v, \theta, \phi))$ , with  $f = \frac{\omega}{2\pi}$ . The sections all appear to have a single peak, indicating that the wavefield has a single component at frequency  $f = 120\text{ Hz}$ , propagating at a speed of  $v = 2381\text{ m/s}$  in the direction  $\theta = 30^\circ$  and  $\phi = 0^\circ$ . Following Haldorsen and Jahren (2020), in evaluating  $|A(\omega, \mathbf{s}(v, \theta, \phi))|^2$ , I used stacking weights in order to constrain the angular wavenumber vector to be within  $\pm 5^\circ$  from the measured particle velocity vector.

Figure 6 shows a wavefield sampled with the same geometry and the same dynamics, except it is assumed that the source is polychromatic with a Ricker wavelet with central frequency of  $120\text{ Hz}$ . A Fourier analysis of these data shows that the data is spatially aliased at frequencies above  $100\text{ Hz}$  (and wavenumber  $\eta > 0.033\text{ m}^{-1}$ ). However, the analysis using equation 15 (results in Figure 7) gives a parametrization very much like what we saw with the monochromatic data: we have a wavefield composed of one single component at frequency centered at  $f = 120\text{ Hz}$ , propagating at a speed of  $v = 2381\text{ m/s}$  in the direction  $\theta = 30^\circ$  and  $\phi = 0^\circ$ .

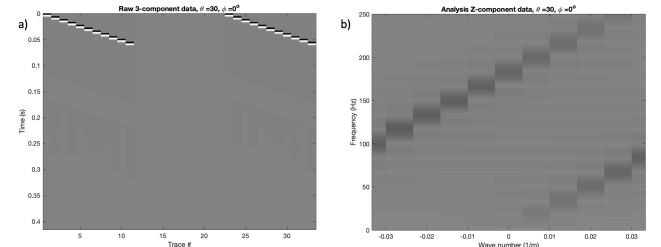


Figure 6: a) a polychromatic wavefield, with a Ricker wavelet at  $120\text{ Hz}$ , sampled by a linear vertical array of the three-component receivers spaced  $15\text{ m}$  apart. The display shows 11 horizontal (x) receivers, followed by 11 horizontal (y) receiver, and 11 vertical (z) receivers. The shallowest receiver is on the left. The wavefield is propagating down along receiver array at an apparent velocity of  $2750\text{ m/s}$ . The wavefield is propagating in the  $(x, z)$  plane (azimuth  $\phi = 0^\circ$ ), at a polar angle of  $\theta = 30^\circ$ . b) a 2D Fourier transform of these waveforms, showing that frequencies above  $f = 100\text{ Hz}$  and wavenumber  $\eta > 0.033\text{ m}^{-1}$  are spatially aliased.

## IMAGING

The most annoying effects from spatial aliasing are seen in imaging artifacts. To illustrate this, I have generated two very simple synthetic data set based on the source-receiver geometry in Figure 8. The 11-receiver vertical array is located at  $x = 0$  along the left edge of the model at a 15 m interval, with the shallowest receiver at 1000 m. The source is located at the surface 1000 m away from the wellhead. The velocity is constant at 2750 m/s and there is a density contrast at the depth of 1200 m. The reflection coefficient at this horizontal interface would be 0.1. The signature of the source is a 120 Hz Ricker wavelet. The two data sets, one 1C and one 3C, are shown in Figure 8. Figure 9 shows the generated data recorded by 1C and 3C receivers.

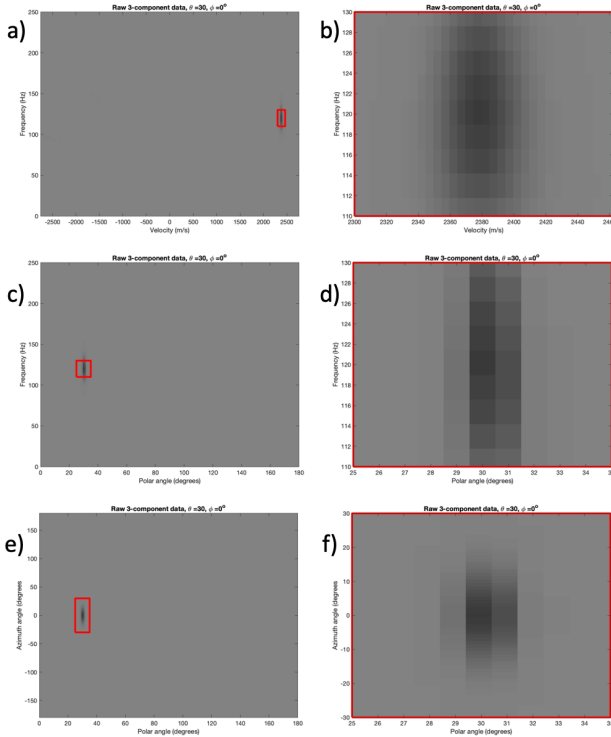


Figure 7: Orthogonal sections through the 4D hypercube  $A(f, \mathbf{s}(v, \theta, \phi))$  from equation 15. Along the right edge of the figure (subplots b), d) and f)) are shown zoomed-in images around the maximum in the larger plots (subplots a), c) and e)) on the left. These sections indicate that the wavefield consists of one single component at a frequency centered at  $f = 120$  Hz, propagating in the direction  $\theta = 30^\circ$  and  $\phi = 0^\circ$  at a speed of  $v = 2381$  m/s (this gives an apparent velocity of  $v = 2750$  m/s).

The imaging into a regular image cube consisting at 1-by-1 m voxel size is done, following Haldorsen and Jahren (2020), by straightforward Kichhoff sums, using weights to correct for uneven distribution of energy flux density over the imaging cube. This process distributes the recorded energy along surfaces of equal traveltime (isochron surfaces). In the simple geometry used here, the isochron surfaces are regular ellipsoids. In an ideal recorded data set, the ellipsoids will cancel everywhere except where they have common tangential planes. At these points the ellipsoids coalesce and form elements of a final image. The Nyquist limit for spatial aliasing is 92 Hz for this setup. The image in Figure 10 obtained from the full 1C receiver array shows some effects from aliasing of frequencies above 92 Hz. When we reduce the array to four receivers at a 45 m interval, the spatial Nyquist frequency becomes 30 Hz, and the incompletely canceled ellipsoids become more obvious.

We repeated the same exercise with the 3C data. Vector migration for P-waves projects the 3C data vector onto a unit vector along the ray connecting reflection points to each receiver. This projection reduces the amplitude of the image by the cosine of the angle between this ray and the propagation direction of the reflected P-wave. Following the recommendation by Haldorsen and Jahren (2020), we use weights to reduce the effective deviation between the ray and the polarization of the data to effectively be  $\pm 5^\circ$ . The image obtained from the 11-level array at a 15 m interval is shown in Figure 11a, and the image obtained from the four-level array at a 45 m interval is shown in Figure 11c. These two images are practically identical.

The reason why the vector imaging works well for VSP data is that one has access to both the timing and location of the seismic source as well as the polarization of the reflected wavefield components as they arrive at the receivers. When applied to estimating the hypocenters of natural or induced earthquakes, one only have access to polarization and relative timing between the different receivers. When the array aperture is small, the necessary additional information comes from identification of S-waves. Haldorsen et al. (2013a) supplement equation 15 for P-waves by

$$\mathbf{A}_S(\omega, \mathbf{s}(v^S, \theta, \phi)) = \sum_m e^{i\omega s^S \cdot \mathbf{x}_m} \sum_n e^{i\omega t} \mathbf{e}_k \times \mathbf{a}(t_n, \mathbf{x}_m), \quad (16)$$

to account for the two shear waves at velocity  $v^S$  and slowness

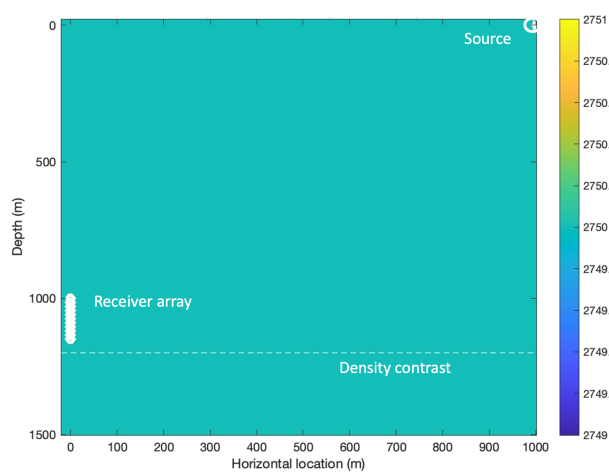


Figure 8: The source-receiver geometry used for generating the data in Figure 9. The 11-receiver vertical array is located at  $x = 0$  along the left edge of the model at a 15 m interval, with the shallowest receiver at a depth of 1000 m. The source is located at the surface, 1000 m away from the wellhead. The velocity is constant at 2750 m/s and there is a density contrast at the depth of 1200 m. The reflection coefficient at this horizontal interface would be 0.1.

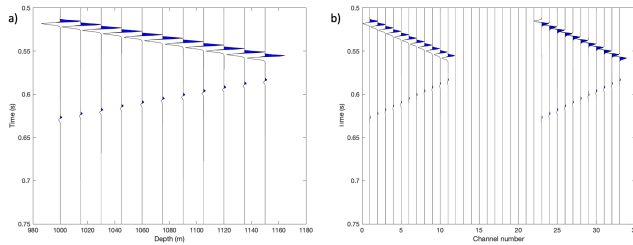


Figure 9: Synthetic data recorded by a 11-level receiver array spaced at 15 m interval: a) the generated data recorded by 1C receivers; b) the same data recorded by 3C (or rather 2C) receivers.

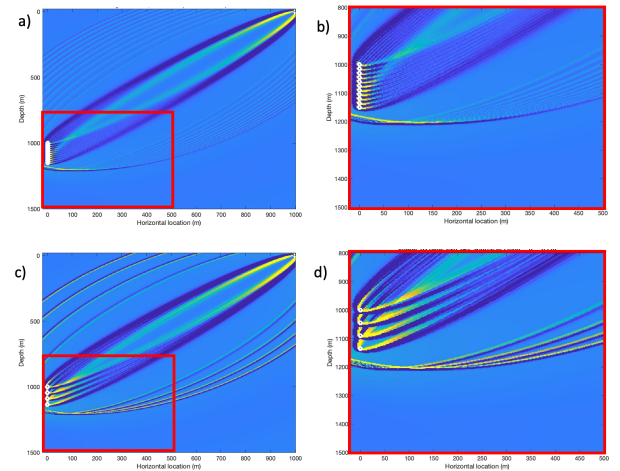


Figure 10: Images obtained from the data recorded by 1C receivers: a) From the full array, 11 receivers at 15 m depth interval. c) From a reduced array, four receiver at 45 m depth interval. Subplots b) and d) are close-ups of subplots a) and c), respectively.

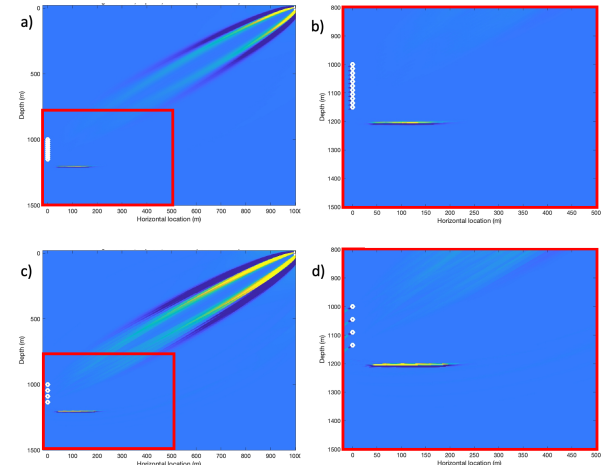


Figure 11: Images obtained from the data recorded by 3C receivers: a) From the full array, 11 receivers at 15 m depth interval. c) From a reduced array, four receiver at 45 m depth interval. Subplots b) and d) are close-ups of subplots a) and c), respectively.

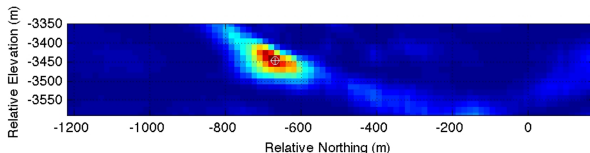


Figure 12: A section through a 3D image showing the likely location of a subsurface source. The image is the results of testing the hypothesis that the perforation shot was located at any given point within a limited 3D volume, and is obtained from data recorded at three shallow and one deep observation wells while a different deep well was perforated. The image is composed of the  $t = 0$  values from the deconvolution of reconstructed signatures for P- and S-waves for the source - consistent with the recorded data after propagation from the source location to each of the receivers.

vector  $\mathbf{s}^S$  (with  $|\mathbf{s}^S| = \frac{1}{v^S}$ ). In an isotropic medium, the S-wave would be polarized perpendicular to the P-wave. Doing this allows them to estimate the hypocenters of an induced microseismic event. The hypocenter location is found by testing the hypothesis that any given location within a limited 3D volume is the origin of the recorded tremors. Figure 12 shows a section through a 3D cube that is the result of testing this hypothesis for data acquired in one deep and three shallow wells, while a different deep well was perforated.

The image is calculated by following the three-step process:

1. Find the P- and S-waves that possibly may have originated at location  $\mathbf{x}$  before being recorded by receiver  $m$  at location  $\mathbf{x}_m$  by projecting the recorded 3C data onto and perpendicular to the ray connecting  $\mathbf{x}$  to  $\mathbf{x}_m$ . Figure 13 shows the projected data for the location with the highest value in the image in Figure 12.
2. Shift the data recorded at station  $m$  by the time  $\mathbf{s} \cdot \mathbf{x}_m$ , aligning the particular component on all recorded data traces. The shifted data are shown in Figure 14.
3. Stack the aligned traces. The resulting estimates of the P-,  $S_v$ - and  $S_h$ -signatures are shown in Figure 15.

The reconstructed  $S_v$ - and  $S_h$ -wave signatures are deconvolved with the reconstructed P-wave signature. When the estimated signatures are correlated and start at the same time, the deconvolved traces will peak at time  $t = 0$ . The image in Figure 12 is obtained by posting the  $t = 0$  value of the corresponding deconvolved data trace at each location  $\mathbf{x}$  in the volume investigated.

## DISCUSSION

We have seen that introducing the direction of particle motion related to a single P-wave into the 4D Fourier transform (equation 11), reduces the Fourier decomposition to an exercise in estimating slowness and amplitude of the components of passing waves. This exercise can be repeated with more complex waveforms, where, e.g., the wavefield  $\mathbf{a}(t, \mathbf{x})$  is composed of  $J$

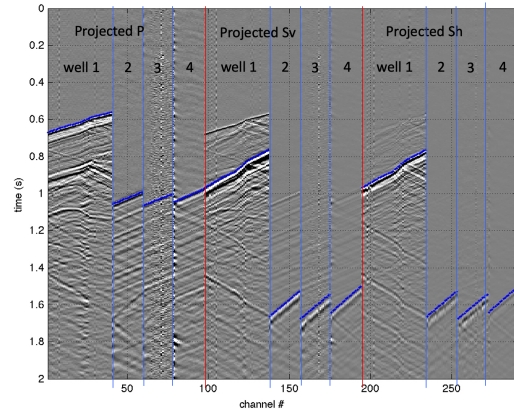


Figure 13: The field data used for generating the image in Figure 12. The data displayed have been projected onto (for the P-wave) and perpendicular to (for the two S-waves) the ray connecting each of the receivers to the source location with the highest value in the image in Figure 8. The wavy near-horizontal blue line represents the traveltimes for the P- and S-waves from the source location to each of the receivers. For the display of this blue line, the arbitrary common reference time has been adjusted so that the blue lines fall near the maxima in the data.

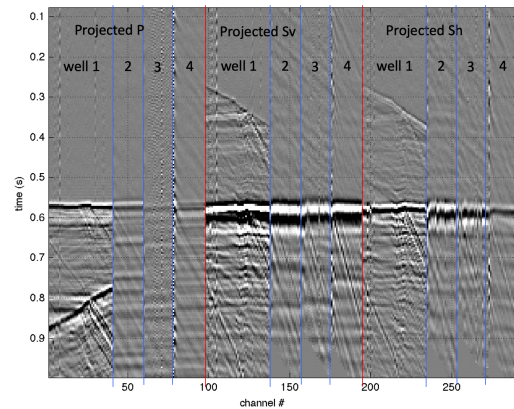


Figure 14: The projected field data in Figure 13, after aligning the data by shifting them according to the traveltimes from the source location to each of the receivers.

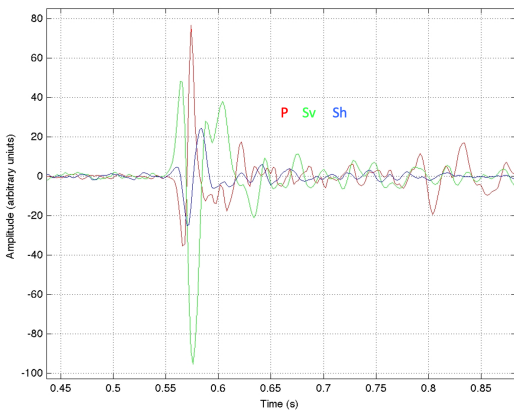


Figure 15: Stacks of the aligned traces in Figure 14. These stacks are the estimates of the P-,  $S_v$ -, and  $S_h$ -signatures for this particular location. For a likely source location, the estimated P-,  $S_v$ -, and  $S_h$ -signatures will be strongly correlated and have the same reference time, meaning that the deconvolution of the S-wave signatures with the P-wave signature will peak at  $t = 0$ . The image in Figure 12 is obtained by posting the  $t = 0$  values of the deconvolved traces at each of the source locations tested.

separate waveforms (a rewrite of equation 8)

$$\mathbf{a}(t, \mathbf{x}) = \sum_{j=1}^J \mathbf{g}_j(\omega) e^{i\omega(\mathbf{s}_j \cdot \mathbf{x} - t)}. \quad (17)$$

Essentially doing this is what allowed Leaney and Esmersoy (1989) to invert three-component VSP data for parameters for a limited number of locally-plane waves. These parameters include amplitudes, slowness, and propagation directions for compressional and shear waves. Whether (or how many of) these elemental waveforms can be independently estimated, has been the issue for discussions in the literature following the publication by Leaney and Esmersoy (1989). The maximum number of different plane waves that can be estimated is likely fundamentally linked to the number of Fourier coefficient in the Fourier expansion - and the minimum separation of wavefield that can be resolved may be limited by the discrete cell size in the 4D Fourier-domain ( $\mathbf{k}, \omega$ ) space.

Measuring both the pressure data and the gradient of the pressure data, Ozbek et al. (2010) use plane-wave expansion to interpolate the spatially aliased pressure data. Rather than interpolate data, the ambition of this study is to argue that it really is not necessary to interpolate the data, as all information relevant for imaging is all in the 3C data. Using the vector of particle motion allows Haldorsen (2002) and Haldorsen et al. (2013b) to reduce the contamination to migrated images from wave-field components of non-relevant polarization, despite insufficient spatial sampling. Relating the particle-motion vector for either P- or S-waves to the direction of wave propagation, allows unambiguous determination of locations for microseismic events (Haldorsen et al., 2013a). The results shown by these authors demonstrate that 3C data contain enough information to allow characterizing the propagating waves. The analyses

reported in this paper supports this, and demonstrate that including the direction of particle motion in the Fourier analysis resolves the problem of spatial aliasing. This all agrees with the simplistic intuition, suggesting that with 3C measurement of the particle motion, one should know where a given wave comes from.

It is important to take away that - for a more complex data set than the simple-minded synthetics used in the present study - plane-wave decomposition does not require that the elemental wave are truly planar, but only that they are locally planar within the aperture used, as demonstrated by Haldorsen and Jahren (2020).

With the new DAS technology, one can inexpensively build large arrays of single-component sensors. However, with single-component sensors, the direction of the incoming wave is not available, and the data will be spatially aliased. Not having to worry so much about spatial aliasing, allows the use of higher frequencies, and therefore potentially enables the generation of higher resolution images from VSP data. This would be particularly useful for borehole-seismic data which tend to contain higher frequencies than surface-seismic data. Complementing a DAS array with sparsely distributed 3C sensors would resolve the directional ambiguities inherent in the DAS data.

Haldorsen et al. (2013a) uses polarization and arrival times to locate microseismic sources. With arrays of pressure sensors or single-axis DAS sensors, the source location would have to be established only from the differences in traveltimes as seen by the individual array sensors. For a linear array of 1C sensors, the time delays alone will image the microseismic source location rotationally symmetric around the axis of the sensor array. Adding a single 3C sensor will introduce a direct measurement of the angle of incidence of the wavefield on the linear array. In addition, the 3C sensor will constrain the source location to be within a plane at a fixed azimuth. Questions that should be addressed in future studies relate to how many 3C sensors should be added, and how should they be spaced. One should also investigate how best to blend 3C and DAS measurements: Should the transverse components of the (sparse?) 3C data be used to simply determine the azimuth plane for imaging, should they be used to add two more components to the DAS data by interpolation, or are there better options, e.g., using wavefield decomposition along the lines discussed in this paper? The best use of supplemental 3C measurements will likely depend on the objectives for acquiring the data.

## CONCLUSIONS

We have shown that by measuring and using all three components of the particle motion in the analysis of the seismic data, the problems associated with "spatial aliasing" can be overcome. Spatial aliasing is about non-uniqueness of wavefield propagation direction for a given frequency. In analyzing several repetitive cycles in the Fourier domain, the correct propagation direction will be one of the choices. The polarization of the measured particle motion can be used to make the correct selection between these multiple choices, and thereby remove the problem of spatial aliasing. Not having to worry so much about spatial aliasing would allow the use of higher frequen-

cies, which potentially would enable the generation of higher resolution images from VSP data.

## REFERENCES

- Artman, B., I. Podladtchikov, and B. Witten, 2010, Source location using time-reverse imaging: *Geophysical Prospecting*, 58, 861-873.
- Bracewell, R. N., 1978, *The Fourier Transform and its Applications*: McGraw-Hill electrical and electronic engineering series.
- Farhadiroushan, M., T. R. Parker, and S. Shatalin, 2009, Method and Apparatus for Optical Sensing: US Patent 9,541,425.
- Haldorsen, J. B. U., 2002, Converted-shear and compressional images using Projection Imaging: 64th Conference and Exhibition, EAGE, Extended Abstracts, F031.
- Haldorsen, J. B. U., N. J. Brooks, M. Milenkovic, 2013a, Locating microseismic sources using migration-based deconvolution: *Geophysics*, 78, no. 5, KS73-KS84.
- Haldorsen, J. B. U., T. Hilton, M. Milenkovic, M. C. Schinelli, L. F. Soares, J. E. Lira, A. Zelia, 2013b, Formation imaging from three-component borehole-seismic data using both space-time relations and wave-field polarization: Presented at the Thirteenth International Congress of the Brazilian Geophysical Society.
- Haldorsen, J. B. U., and L. Jahren, 2020, Imaging Below a Complex Overburden with Borehole-Seismic Data: *Geophysics*, 85, no. 3, S135-S150.
- Leaney, W. S., and C. Esmersoy, 1989, Parametric Decomposition of Offset VSP Wave Fields: 59th Annual International Meeting, SEG, Expanded Abstracts, 26-28.
- Ozbek, A., M. Vassallo, K. Ozdemir, D. van Manen, and K. Eggenberger, 2010, Crossline wavefield reconstruction from multicomponent streamer data: Part 2 - Joint interpolation and 3D up/down separation by generalized matching pursuit: *Geophysics*, 75, no. 6, 1ND-Z138.